Transferable local pseudopotentials for magnesium, aluminum and silicon

Chen Huang[a] and Emily A. Carter*[b]

Received 19th June 2008, Accepted 2nd September 2008
First published as an Advance Article on the web 20th October 2008
DOI: 10.1039/b810407g

One obstacle in orbital-free density functional theory (OF-DFT) is the lack of accurate and transferable local pseudopotentials (LPSs). In this work, we build high quality LPSs by inverting Kohn–Sham (KS) equations on bulk valence electron densities to obtain an atom-centered local pseudopotential. With this approach, we build LPSs for Mg, Al, and Si, and then test them in KS DFT calculations of static bulk properties for several Mg, Al, and Si bulk structures as well as β''-Al_3Mg. Our Mg, Al, and Si LPSs produce correct ground state properties and phase orderings. These LPSs are then tested in KS-DFT calculations of surface energies for several low-index Mg and Al surfaces, point defect properties in hexagonal-close-packed (hcp) Mg, face-centered cubic (fcc) Al, and diamond Si, and stacking fault energies in fcc Al. All of these LPS results agree quantitatively with the results from nonlocal pseudopotentials with errors less than or equal to 40 meV per atom. Finally, we perform OF-DFT calculations for various Mg and Al structures, employing the Wang–Govind–Carter (WGC) nonlocal kinetic energy density functional (KEDF). The OF-DFT results generally agree well with the corresponding KS-DFT results. With our new Mg and Al LPSs and the WGC KEDF, OF-DFT now provides a practical method for accurate, large-scale first principles simulations of main group metals and their alloys.

1. Introduction

Among various first-principles quantum mechanics methods, Kohn–Sham density functional theory (KS-DFT),[1] which is based on the Hohenberg–Kohn (HK) theorems,[2] strikes a good balance between accuracy and computational cost. Unfortunately, the cost of KS-DFT typically scales roughly cubically with system size, although methods that scale linearly for nonmetals above O(100) atoms are now available.[3] The situation is worse for metals, since the conventional cubic scaling can be accompanied by a large prefactor due to the need for dense Brillouin zone sampling. Consequently, it is impractical at present to use KS-DFT to simulate thousands of atoms. On the other hand, such large samples can be studied readily with orbital-free density functional theory (OF-DFT), which is also based on the HK theorems but requires much less computational time, with a cost that can be made to scale linearly with system size. OF-DFT simulations of thousands of sodium atoms was demonstrated already a decade ago.[4]

Although OF-DFT is impressively efficient computationally, it is difficult to obtain the accuracy of KS-DFT within OF-DFT. The lack of orbitals in OF-DFT renders two terms in the total energy quite challenging to represent accurately: the kinetic energy and the ion-electron potential energy (by "ion" we mean the nucleus plus core electrons, which are typically represented together as a pseudopotential acting on the valence electrons). KS-DFT introduces orbitals, which provides the means to evaluate the electron kinetic energy in terms of the exact kinetic energy of non-interacting electrons (the correction to this kinetic energy for interacting electrons is subsumed into the exchange–correlation functional). By contrast, OF-DFT expresses the kinetic energy only in terms of the electron density, in a kinetic energy density functional (KEDF). Recent advances in KEDF theory include the development of nonlocal KEDFs that reproduce the linear response of a uniform electron gas.[5–9] For example, OF-DFT with the Wang–Govind–Carter (WGC) KEDF[8] reproduces KS kinetic energies of simple main group metals very well. Consequently, properties of bulk aluminum, magnesium, and an Al–Mg alloy can be predicted by OF-DFT almost as accurately as by KS-DFT.[8,10,11] However, for other types of materials, an accurate KEDF remains to be developed, limiting the scope of what OF-DFT can currently be used to study.

Besides the need for an accurate KEDF in OF-DFT, accurate and transferable electron-ion local pseudopotentials (LPSs) are also required to perform a meaningful OF-DFT calculation. Unlike KS-DFT in which norm-conserving[12] and ultra-soft nonlocal pseudopotentials (NLPSs),[13] and the related nonlocal projector augmented-wave method[14] have been widely used, currently only LPSs can be used in OF-DFT, as no KS orbitals exist in OF-DFT onto which different angular momentum-dependent potentials can be projected. Many schemes have been proposed for LPS construction. One approach is to design an analytic form for the LPS,[15–20] for which the parameters are optimized to fit to experimental data or some other constraints. Another strategy is a direct numerical method. Here the valence electron density is first generated from a KS-DFT calculation using a NLPS[21–23] or is generated by defining the valence density

[a] *Department of Physics, Princeton University, Princeton, New Jersey, 08544, USA. E-mail: chenh@Princeton.edu*
[b] *Department of Mechanical and Aerospace Engineering and Program in Applied and Computational Mathematics, Princeton University, Princeton, New Jersey, 08544-5263, USA. E-mail: eac@Princeton.edu*

profile manually.[24] A first attempt in this direction inverted the orbital-free HK equation[2] directly, employing a KEDF and the KS-NLPS valence electron density[25] to derive a LPS. A related OF method to build a LPS for lithium involved embedding a lithium ion into an electron gas.[26]

The accuracy of the latter two methods is limited by the quality of the KEDF used. An alternative procedure is to invert the KS-DFT equations instead of the HK equation, so as to utilize the exact non-interacting kinetic energy operator. A local KS effective potential is then derived that is able to reproduce the valence electron density. Then this potential is unscreened by subtracting off the electron–electron Coulomb repulsion and exchange–correlation potentials to obtain the ionic external potential. If the valence electron density is generated from a single atom,[21,24] then the ionic potential is already the LPS for that atom. If the density is generated in a bulk crystalline environment,[22,23,25] then the bulk crystal's structure factor is needed to further convert the ionic external potential into an atom-centered ionic potential, which is the LPS of that atom.

The method presented in this paper is of the second type described above, and is based on the previous work of Zhou *et al.*[22] They referred to this kind of LPS as a "bulk-derived local pseudopotential" (BLPS), and demonstrated for silicon that the Si BLPS was more transferable than the Si LPS built from the valence electron density of a Si atom. However, Zhou *et al.*'s Si BLPS still has two remaining deficiencies: (i) it gives an incorrect energy ordering for several Si bulk structures relative to predictions from a NLPS (the latter is presumed to be more accurate) and (ii) it requires a large kinetic energy cutoff to converge the planewave basis set. To address the above two problems, we outline two improvements on the method of Zhou *et al.*, both of which involve how the tails of BLPS are handled in real and reciprocal spaces. The new Si BLPS obtained with our improved scheme is able to give the correct energy ordering for all Si bulk structures studied in the work of Zhou *et al.*, and is a much "softer" LPS, allowing convergence of the planewave basis set at much smaller kinetic energy cutoffs. The same approach is also applied to build Mg and Al BLPSs.

This paper is organized as follows. First, we outline how the KS equations are inverted, a key step in building BLPSs. Then we present a detailed procedure for building a BLPS, with numerical details given afterwards. The resulting Mg, Al, and Si BLPSs are then presented and analyzed. The performance of our BLPSs is first compared within KS-DFT to results from NLPSs. Last, we compare results of OF-DFT calculations using our BLPSs and the WGC KEDF to KS-DFT for various Mg and Al systems.

2. Inverting the KS equations

Our first task is to find a local external potential that can reproduce a given electron density. According to the first HK theorem,[2] there exists a unique local external potential associated with a given *v*-representable electron density. To obtain this local external potential, we first invert the KS equations to extract a local KS effective potential able to reproduce the target electron density.

Many ways have been proposed to invert the KS equations. One is an iterative method,[27] which was used by Zhou *et al.* in building Si[22] and Ag[23] BLPSs. Here we use a different technique: the direct optimization method developed by Wu and Yang.[28] A brief introduction is given below.

In the Wu–Yang method, a functional $W[v_{\mathrm{eff}}(\boldsymbol{r}),\rho_0(\boldsymbol{r})]$ is defined as

$$W[v_{\mathrm{eff}}(\boldsymbol{r}),\rho_0(\boldsymbol{r})] = T_{\mathrm{s}}[v_{\mathrm{eff}}(\boldsymbol{r})] + \int \mathrm{d}\boldsymbol{r}(\rho(\boldsymbol{r}) - \rho_0(\boldsymbol{r}))v_{\mathrm{eff}}(\boldsymbol{r}) \quad (1)$$

where $\rho_0(\boldsymbol{r})$ is the target electron density. With a trial local KS effective potential $v_{\mathrm{eff}}(\boldsymbol{r})$, we solve the KS equations to get the total kinetic energy $T_{\mathrm{s}}[v_{\mathrm{eff}}(\boldsymbol{r})]$ and the electron density $\rho(\boldsymbol{r})$. Then we insert these $T_{\mathrm{s}}[v_{\mathrm{eff}}(\boldsymbol{r})]$, $\rho(\boldsymbol{r})$, and $v_{\mathrm{eff}}(\boldsymbol{r})$ back into eqn (1) to evaluate the functional $W[v_{\mathrm{eff}}(\boldsymbol{r}),\rho_0(\boldsymbol{r})]$. The optimal $v_{\mathrm{eff}}(\boldsymbol{r})$ will maximize the functional $W[v_{\mathrm{eff}}(\boldsymbol{r}),\rho_0(\boldsymbol{r})]$, which in turn will be the $v_{\mathrm{eff}}(\boldsymbol{r})$ that reproduces the target electron density $\rho_0(\boldsymbol{r})$. Specifically, we expand $v_{\mathrm{eff}}(\boldsymbol{r})$ in a basis set $g_t(\boldsymbol{r})$ as

$$v_{\mathrm{eff}}(\boldsymbol{r}) = \sum_t b_t g_t(\boldsymbol{r})$$

The gradient of W with respect to b_t is

$$\frac{\partial W}{\partial b_t} = \int d\boldsymbol{r}(\rho(\boldsymbol{r}) - \rho_0(\boldsymbol{r}))g_t(\boldsymbol{r})$$

We have implemented this direct optimization method in the ABINIT code.[29] In the code, $v_{\mathrm{eff}}(\boldsymbol{r})$ is expanded in a plane wave basis set and the coefficients are optimized to minimize the functional $-W[v_{\mathrm{eff}}(\boldsymbol{r}),\rho_0(\boldsymbol{r})]$ using a conjugate gradient optimization code.[30] We note that the Fourier component of $v_{\mathrm{eff}}(\boldsymbol{r})$ at $\boldsymbol{q} = 0$, denoted as $\tilde{v}_{\mathrm{eff}}(\boldsymbol{q} = 0)$, can be set to any value, which just shifts the entire $v_{\mathrm{eff}}(\boldsymbol{r})$ by a constant. Because the shifted $v_{\mathrm{eff}}(\boldsymbol{r})$ yields the same electron density, we manually set $\tilde{v}(\boldsymbol{q} = 0)$ to zero during the optimization. Later, $\tilde{v}_{\mathrm{eff}}(\boldsymbol{q} = 0)$ is adjusted manually, since its value affects $\tilde{v}_{\mathrm{eff}}(\boldsymbol{q})$ at low but nonzero $\boldsymbol{q}$ values due to the spline fit used.

3. Building a BLPS

The first step in building a BLPS is to generate the target bulk electron densities used during inverting the KS equations with the Wu–Yang method. We select the face-centered cubic (fcc), body-centered cubic (bcc), simple cubic (sc), and diamond (dia) structures in order to generate a wide range of bulk electron densities. These four particular structures span a range of coordination numbers from 12 for fcc down to diamond's 4, with sc and bcc exhibiting intermediate coordination numbers of 6 and 8, respectively. By generating densities over this range of coordination, we anticipate that our BLPSs should be able to work well in both close-packed and more open bulk environments. The target bulk electron densities are obtained by solving the KS-DFT equations using NLPSs with bulk crystal structures in which both cell vectors and ion positions have been optimized. Numerical details of these calculations can be found in the next section.

We then invert the KS equations using these target bulk electron densities to obtain the local KS effective potentials $v_{\mathrm{eff}}(\boldsymbol{r})$ for these bulk structures using the Wu–Yang method described above. Since we need to solve the KS equations

Table 1 Numerical details in this work. E_{cut} and E_{conv} refer to both KS-DFT and OF-DFT calculations. $\boldsymbol{k}$-point meshes, Fermi surface smearings, and E_k are only for KS-DFT. E_{cut} is the kinetic energy cutoff used to truncate the plane-wave basis set. E_{smear} is the smearing width in the Fermi–Dirac smearing scheme. E_{conv} and E_k are the convergence of the total energy per atom with respect to E_{cut} and $\boldsymbol{k}$-point meshes, respectively

System	E_{cut}/eV	E_{conv}/meV per atom	E_{smear}/eV	$\boldsymbol{k}$-point mesh	E_k/meV per atom
sc, bcc, and fcc Al and Mg	800	<0.1	0.1	$20 \times 20 \times 20$	<1
Diamond and hcp Al and Mg	800	<0.1	0.1	$12 \times 12 \times 12$	<1
Al_3Mg	600	<0.1	0.1	$20 \times 20 \times 20$	<1
cbcc, β-tin, hcp, and bct5 Si	1000	<0.1	0.1	$12 \times 12 \times 12$	<1
sc, bcc, and fcc Si	1000	<0.5	0.1	$16 \times 16 \times 16$	<1
Diamond and hd Si	1000	<0.5	Not used	$12 \times 12 \times 12$	<1
Vacancy formation energy in fcc Al	800	<0.1	0.1	$8 \times 8 \times 8$	<2
Vacancy migration energy in fcc Al	600	<0.1	0.1	$6 \times 6 \times 6$	<5
Vacancy formation energy in hcp Mg	800	<0.1	0.1	$4 \times 4 \times 4$	<2
Vacancy migration energy in hcp Mg	600	<0.1	0.1	$4 \times 4 \times 4$	<2
Al fcc(111) surfaces	800	<0.1	0.1	$18 \times 18 \times 1$	<1
Al fcc(100) and fcc(110) surfaces	800	<0.1	0.1	$20 \times 20 \times 1$	<1
Mg hcp(0001) surface	800	<0.1	0.1	$12 \times 12 \times 1$	<1
Mg bcc(100) and bcc(110) surfaces	800	<0.1	0.1	$20 \times 20 \times 1$	<1
Stacking fault energies in fcc Al	480	<0.1	0.1	$10 \times 10 \times 1$	<0.5
Vacancy formation and migration energy in diamond Si using LPSs	760	<0.1	Not used	$2 \times 2 \times 2$	<1.3
Vacancy formation and migration energy in diamond Si using ultrasoft NLPS	500	<0.3	Not used	$2 \times 2 \times 2$	<1.3

again for every trial local KS effective potential in the direct optimization method, the settings of $\boldsymbol{k}$-point meshes, Fermi–Dirac smearing widths, and planewave kinetic energy cutoff values used are the same as those used in generating the target bulk electron densities (see Table 1 and section 4).

After inverting the KS equations, we unscreen the local KS effective potential by subtracting off the electron–electron Coulomb repulsion and exchange–correlation potentials to extract out the bulk ionic potential

$$v^{\text{bulk}}(\boldsymbol{r}) = v_{\text{eff}}(\boldsymbol{r}) - \frac{\delta J[\rho]}{\delta \rho(\boldsymbol{r})} - \frac{\delta E_{\text{xc}}[\rho]}{\delta \rho(\boldsymbol{r})}$$

We then Fourier transform $v^{\text{bulk}}(\boldsymbol{r})$ to obtain the atom-centered ionic potential $v^{\text{atom}}(\boldsymbol{q})$ in reciprocal space by dividing by the structure factor $S(\boldsymbol{q})$ of each bulk crystal

$$v^{\text{atom}}(q) = \frac{v^{\text{bulk}}(\boldsymbol{q})}{S(\boldsymbol{q})} \tag{2}$$

where $q = |\boldsymbol{q}|$. To avoid the singularity of $v^{\text{atom}}(q)$ at $q = 0$, we work with the non-Coulombic part of $v^{\text{atom}}(q)$

$$v^{\text{nc}}(q) = v^{\text{atom}}(q) + \frac{4\pi Z}{q^2}, \tag{3}$$

where Z is the pseudocharge (nuclear charge minus core electron charge). Thus Z is 2 for Mg, 3 for Al, and 4 for Si.

4. Calculational details

Periodic KS-DFT calculations to obtain the bulk densities for BLPS construction, static bulk properties for Mg, Al, and Si, surface energies for Mg and Al, stacking fault energies for fcc Al, and defect formation energies in hcp Mg and fcc Al are performed using the ABINIT planewave DFT code.[29] Periodic OF-DFT calculations are done with the FORTRAN90-based code, PROFESS (Princeton Orbital-Free Electronic Structure Software), developed in our group.[31] The OF-DFT code also uses a planewave basis set. In all KS-DFT and OF-DFT calculations, we use the local density approximation (LDA) for electron exchange and correlation, derived from the quantum Monte Carlo results of Ceperley and Alder[32] as parameterized by Perdew and Zunger.[33]

Calculations with the ABINIT code are done using Troullier–Martins (TM) NLPSs,[34] generated with the FHI98PP code.[35] We use the default core cutoff radii in the FHI98PP code for Mg and Si. The Mg TM-NLPS has core cutoff radii of 2.087, 2.476, 2.476, and 2.476 bohr for s-, p-, d-, and f- channels, respectively. The Si TM-NLPS has core cutoff radii of 1.704, 1.878 and 2.02 bohr for s-, p-, and d- angular momentum channels, respectively, the same settings as in the work of Zhou *et al.*[22] For the Al TM-NLPS, we set the core cutoff radii to be 2.1 bohr for all angular momentum channels (the default core cutoff radii are 1.790, 1.974, 2.124, and 2.124 bohr for s-, p-, d-, and f- angular momentum channels, respectively). Use of the default core cutoff radii for the Al TM-NLPS produced negligible changes in the Al BLPS's softness and quality, justifying our simpler choice of 2.1 bohr for all channels. For all Mg, Al, and Si TM-NLPSs, the d-angular momentum channel is used as the local pseudopotential to construct the Kleinman–Bylander[36] form of the NLPSs. In all cases, the NLPSs are unscreened with LDA exchange–correlation. In OF-DFT calculations, we use Madden and coworkers' LPS for Mg,[25] Goodwin and coworkers' LPS for Al,[19] Zhou and coworkers' Si BLPS,[22] and our new Mg, Al, and Si BLPSs from this work. Some KS-DFT calculations are performed with the CASTEP code,[37] with which we use its default ultrasoft NLPSs.

All numerical details are summarized in Table 1, including planewave kinetic energy cutoffs used in both KS and OF-DFT. For consistency, we used the highest planewave cutoff required for convergence of any pseudopotential employed for a given system in both KS and OF calculations. We use primitive cells throughout this work: one atom in fcc, bcc, and sc structures; two atoms in dia, body-centered tetragonal 5 (bct5), hexagonal-close-packed (hcp), and β-tin structures;

four atoms in the hexagonal diamond (hd) structure; and eight atoms in the complex bcc (cbcc) structure, as given in ref. 22.

We use Fermi–Dirac smearing with a width of 0.1 eV to smooth out the Fermi surface for Mg, Al, and all metallic phases of Si (cbcc, β-tin, bct5, sc, bcc, and fcc Si). No smearing is used for the Si dia and hd phases, both of which are semiconductors. All $\boldsymbol{k}$-point meshes in the Brillouin zone are generated using the Monkhorst–Pack method.[38]

In all OF-DFT calculations, the WGC KEDF[8] is used with the parameters: $\gamma = 2.7$, $\alpha = (5+\sqrt{5})/6$ and $\beta = (5-\sqrt{5})/6$. Those parameters are optimum for bulk Al.[8] Previous work demonstrated that these parameters also work well for Mg and β''-Al_3Mg.[10] To render evaluation of the WGC KEDF linear scaling, we compute it approximately by Taylor expanding the WGC KEDF kernel around the relevant average bulk electron density.[8] In the case of Al and Mg surfaces, the kernel of the WGC KEDF is Taylor expanded around the average electron density of bulk fcc Al or hcp Mg at their respective equilibrium volumes.

All calculations of bulk crystal properties start by obtaining optimized structures, by relaxing cell vectors and ion positions. Thresholds below which the stress tensor elements and forces on ions are considered minimized are 5×10^{-7} hartree bohr^{-3} and 5×10^{-5} hartree bohr^{-1}, respectively. Once the equilibrium cell vectors are determined, the ratios between cell vectors are kept fixed during changes in the bulk volume used to calculate bulk moduli, equilibrium volumes, and energies. We compress and expand the unit cell isotropically from $0.95V_0$ to $1.05V_0$, where V_0 is the equilibrium volume. Then the energy *versus* volume curve is fitted to Murnaghan's equation of state,[39] which yields the bulk modulus.

Point defects in Al, Mg, and Si are set up as follows. A vacancy in bulk fcc Al is constructed by putting eight Al fcc cubic unit cells together in a $2 \times 2 \times 2$ fashion to form a supercell with 32 Al atoms. One Al atom is then removed from one of the supercell's four corners to create a vacancy. The vacancy formation energy calculated with this 32-site cell is converged to within 0.04 eV with respect to cell size.[40] To construct a vacancy in hcp Mg, 18 Mg hcp primitive cells are put together in a $3 \times 3 \times 2$ fashion and then one Mg atom is removed from one of the supercell's corners. This 35-atom supercell yields a reasonable vacancy formation energy.[41]

To construct the vacancy and interstitial defects in a Si diamond structure, we use the same supercell as in the work of Zhou *et al.*:[22] a cubic Si supercell with 64 lattice sites constructed by putting 8 cubic unit cells together in a $2 \times 2 \times 2$ fashion. One vacancy is created by removing the atom at the center of the supercell. The interstitial defect is created by inserting an extra atom at the tetrahedral site. Both the supercell and ion positions are fixed during the calculations. Due to the presence of dangling bonds, spin-polarized KS-DFT is employed to calculate defect formation energies using the CASTEP code.

The lattice vectors of each supercell are fixed to the equilibrium bulk lattice vectors, but the ion positions are fully relaxed in the presence of these vacancies. We use these same supercells to calculate activation energies for vacancy migration between nearest neighbor sites. The initial and final states for migration are obtained by fully relaxing the ions with the supercell lattice vectors fixed.

The vacancy formation energy (E_{vf}) is calculated as in Gillan's work[42]

$$E_{\mathrm{vf}} = E\left(N-1, 1, \frac{N-1}{N}\Omega\right) - \frac{N-1}{N}E(N,0,\Omega),$$

and the interstitial formation energy (E_{if}) is calculated as

$$E_{\mathrm{if}} = E\left(N+1, 1, \frac{N+1}{N}\Omega\right) - \frac{N+1}{N}E(N,0,\Omega),$$

where $E(n,m,\Omega)$ is the total energy for the cell of volume Ω with n atoms and m defects.

In KS-DFT, the vacancy migration energy is calculated using the linear/quadratic synchronous transit method[43] in the CASTEP code, with a maximum force threshold of 0.05 eV Å^{-1}. In OF-DFT, the vacancy migration energy is calculated using the climbing-image nudged elastic band (CINEB) method[44,45] implemented in PROFESS code, with a maximum force threshold of 0.01 eV Å^{-1}.

We model the Al fcc(110), (100), and (111) surfaces with seven, five, and five layers of Al atoms, respectively, and with vacuum layer thicknesses of 12.6, 11.9, and 13.7 Å, respectively. These models have been tested to give reasonable Al surface energies.[8] Mg hcp(0001), bcc(001), and bcc(110) surfaces are modeled with nine, seven, and five layers of Mg atoms, respectively, and vacuums of 12.4 Å, 14.8 Å, and 14.8 Å, respectively. Mg and Al surface unit cells contain only one atom in the lateral direction, with lateral lattice constants taken from the equilibrium bulk structure but with all ions relaxed.

Surface energies are defined as

$$\sigma = (E_{\mathrm{slab}} - NE_0)/(2A),$$

where E_{slab} is the total energy of slab, E_0 is the total energy per atom of bulk hcp Mg or fcc Al at its equilibrium volume, N is the number of atoms in slab, and A is the lateral area of each slab. The factor of 2 in the denominator is due to the creation of two surfaces upon forming the slab.

The phase transition pressure in Si is calculated using the common tangent rule

$$\left.\frac{\mathrm{d}E}{\mathrm{d}V}\right|_{\mathrm{phase1}} = \left.\frac{\mathrm{d}E}{\mathrm{d}V}\right|_{\mathrm{phase2}} = -P_{\mathrm{trans}}.$$

To calculate stacking fault energies in bulk fcc Al, we use the same setup (Fig. 1) as in Bernstein and Tadmor's work.[46] The layers in the illustration marked by arrows translate laterally together. After each small translation step, we perform calculations by relaxing ion positions only in the z-direction with lattice vectors in the x–y plane fixed to the bulk fcc Al equilibrium values, but the lattice vector in the z-direction is relaxed. Unit cells contain only one atom in the lateral direction, with 20 [setup (a)] and 22 [setup (b)] atoms in the z-direction.

We use the primitive unit cell of β''-Al_3Mg, which contains three Al atoms and one Mg atom, to model the bulk alloy. The alloy formation energy per atom is defined as

$$\Delta E_{\mathrm{f}} = (E_{\mathrm{Al_3Mg}} - 3E_{\mathrm{Al}} - E_{\mathrm{Mg}})/4,$$

where $E_{\mathrm{Al_3Mg}}$ is the total energy of the primitive cell of the β''-Al_3Mg alloy at its equilibrium volume. E_{Mg} and E_{Al} are the

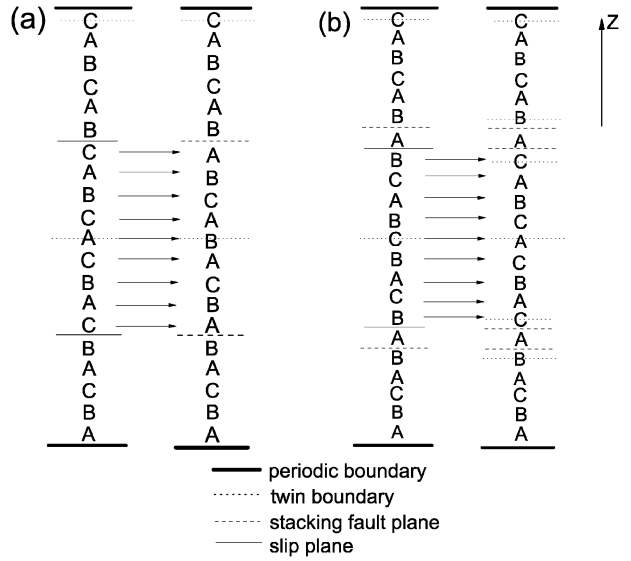

Fig. 1 Illustration (after Bernstein and Tadmor[46]) of the atomic layer configuration setup used to compute various stacking fault energies in fcc Al. Setup (a) and setup (b) are used to calculate the stacking fault energy changes from $d = 0$ to $d = 1.0$ and from $d = 1.0$ to $d = 2.0$ in Fig. 4, respectively. "A, B, C" denote the atomic layers in fcc Al.

total energy per atom of hcp Mg and fcc Al at their equilibrium volumes.

5. Results

5.1 Bulk-derived LPS

The non-Coulombic BLPS $v^{nc}(q)$ and the complete BLPS $v^{atom}(q)$ of Mg, Al, and Si are displayed in Fig. 2. It is evident that for each element, the data points from different bulk structures almost constitute a common curve. This finding confirms our basic assumption underlying this work: there exists a common local pseudopotential suitable for describing a wide variety of structural environments, as illustrated here by fcc, bcc, sc, and dia structures.

With just the data points in Fig. 2, we still cannot complete $v^{nc}(q)$ because we lack the data point at $q = 0$. As explained above, $v^{nc}(q = 0)$ is undetermined at this stage. So we treat $v^{nc}(q = 0)$ as a fitting parameter. With a trial value for $v^{nc}(q = 0)$, we can complete $v^{nc}(q)$ by smoothing these data points in Fig. 2 using the least-squares method and then applying piecewise cubic Hermite interpolation to the smoothed data points.[47] Subsequently, we add back the Coulombic part to $v^{nc}(q)$ to obtain a trial BLPS in the q-space: $v^{BLPS}(q)$.

All Mg, Al, and Si data for $v^{BLPS}(q)$ exhibit a small oscillating tail along the q-axis, as shown in the insets of Fig. 2. Mg exhibits the largest amplitude oscillations. Those oscillating tails in q-space can cause oscillating tails in real space when we Fourier transform $v^{BLPS}(q)$:

$$v^{BLPS}(r) = \frac{1}{2\pi^2}\int_0^\infty v^{BLPS}(q)\frac{q\sin(qr)}{r}\mathrm{d}q.$$

To solve this problem, we simply multiply our $v^{BLPS}(q)$ with a cutoff function $f(q)$. We use the same cutoff function as in the work of Goodwin *et al.*[19]

$$f(q) = \exp(-(q/q_c)^6),$$

where we set q_c to be the third zero of the $v^{BLPS}(q)$. We find that increasing q_c, *i.e.*, including more of the tail in the $v^{BLPS}(q)$, does not improve the quality of the BLPSs. In practice q_c is set to 6.1, 5.6, and 6.14 bohr^{-1} for Mg, Al, and Si, respectively. We have also explored using a step function as the cutoff function. The change in the BLPS quality due to different cutoff functions is negligible, but use of the cutoff function greatly reduces the kinetic energy cutoff required to converge the plane wave basis.

In addition to optimizing the reciprocal space asymptotic behavior, we also need to determine the real space Coulombic tail of the BLPS. Zhou *et al.*[22] enforced a Coulombic tail onto $v^{BLPS}(r)$ beyond a certain point r_c. They argued that the smaller r_c was, the more transferable the final $v^{BLPS}(r)$ should be, as is commonly found for NLPSs. In actuality, $v^{BLPS}(r)$ should have its own intrinsic Coulombic tail, but it cannot be accurately recovered after Fourier transforming $v^{BLPS}(q)$ into real space because of the dearth of data at low enough $\boldsymbol{q}$-vectors. A systematic means to determine the radial cutoff beyond which we recover the intrinsic Coulombic tail in real space is needed.

We now describe a detailed method to determine r_c and $v^{nc}(q = 0)$, the only two fitting parameters in our method. We take Al as an example here; the method is the same for Mg and Si. First we set r_c to a large value; in practice r_c is set to 12 bohr for all three elements. In the second step, we fix r_c and tune $v^{nc}(q = 0)$ to see if we can obtain a $v^{BLPS}(r)$ that yields bulk moduli and equilibrium volumes in good agreement with the corresponding Al TM-NLPS results for all bulk structures used in building the Al BLPS, *i.e.*, the Al fcc, bcc, sc, and dia structures. We also aim to reproduce with this $v^{BLPS}(r)$ the energy differences between these bulk structures calculated with the Al TM-NLPS. If we fail to find a $v^{nc}(q = 0)$ to make a $v^{BLPS}(r)$ that satisfies the above requirements, we conclude that the current r_c is too large and we decrease r_c by 0.5 bohr. With this new r_c, we repeat the second step until we find a combination of r_c and $v^{nc}(q = 0)$ that produces a good $v^{BLPS}(r)$. This $v^{BLPS}(r)$ is our final BLPS with a Coulombic tail starting at r_c. The r_c of the final Mg, Al, and Si BLPSs (shown in Fig. 3) are 8.5, 6.5, and 10.5 bohr, respectively.

When building the BLPS, we only require that the final BLPS reproduces bulk properties of a subset of structures that agree well with results using the TM-NLPS. Below we test the transferability of the BLPS in calculations of other bulk structures, surface energies, defect energies, and the Al_3Mg alloy formation energy. None of the results from these latter tests are used to determine r_c and $v^{nc}(q = 0)$.

5.2 Comparing the BLPS with other PSs in KS-DFT

In this section, we will first compare KS-DFT predictions of various bulk, defect, and interface properties of Mg, Al, and Al_3Mg using the new Mg and Al BLPSs *versus* using TM-NLPSs, in order to evaluate the accuracy and transferability

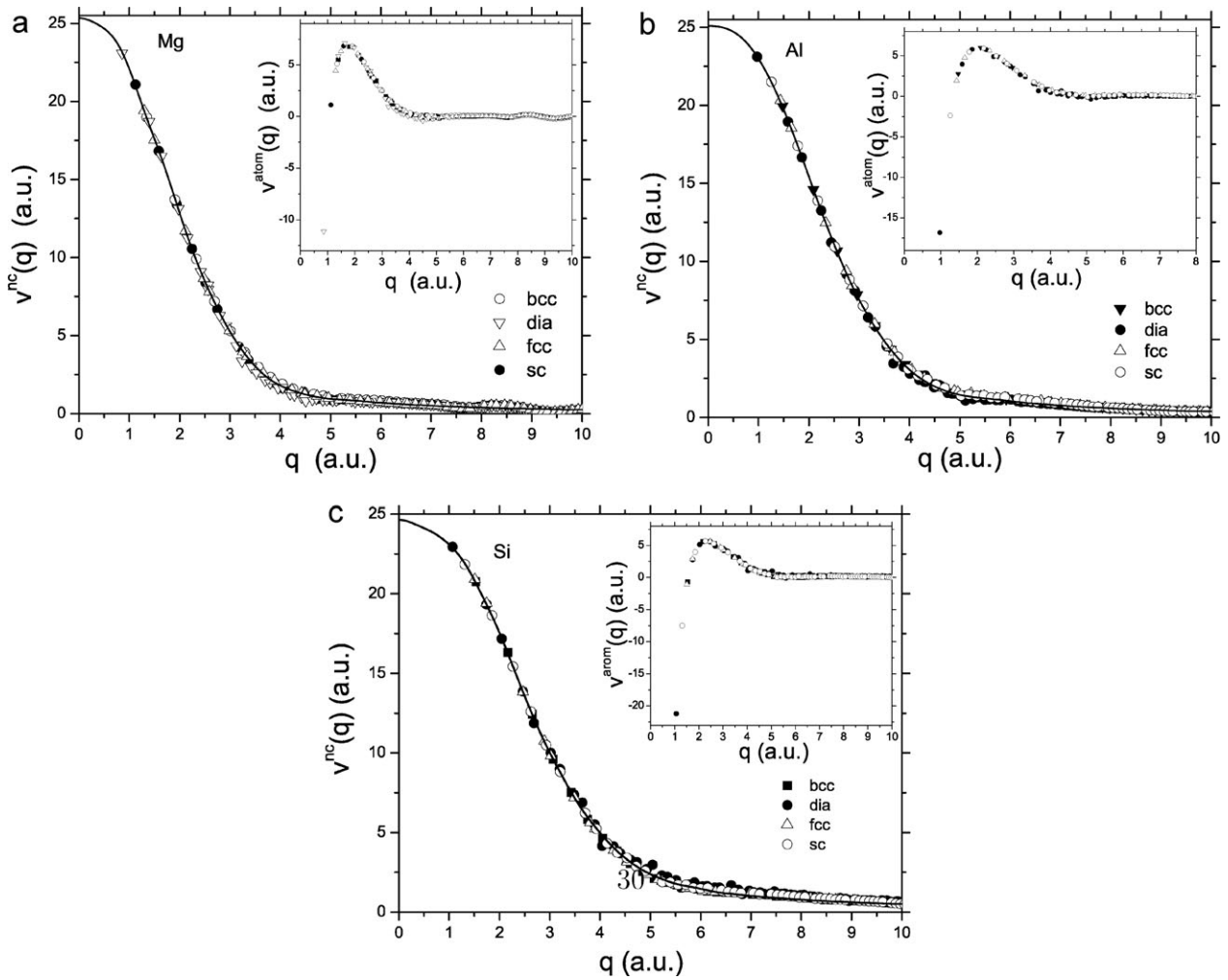

Fig. 2 The main graphs display $v^{nc}(q)$ [eqn (3)], the non-Coulombic part of the final (a) Mg, (b) Al and (c) Si BLPSs in reciprocal space (solid lines). The data points are discrete values of atom-centered local pseudopotentials generated from different bulk structures (see legends). Data points in the insets are the complete atom-centered local pseudopotentials [eqn (2)] containing the Coulombic part. For each of the three elements, the data points from different bulk structures almost constitute a common curve.

of these Mg and Al BLPSs. We also compare the quality of our BLPSs to Madden and coworkers' LPS for Mg[25] and Goodwin and coworkers' for Al.[19] The quality of our new Si BLPS is tested afterward.

5.2.1 Static bulk properties. As shown in Table 2, static bulk properties calculated using our Mg and Al BLPSs are in exellent agreement with those calculated using TM-NLPSs, except for the bulk modulus of sc Mg and the equilibrium volume of dia Mg, where the deviation is more significant. The TM-NLPS energy differences between any two bulk structures are reproduced by our BLPSs with an error of <40 meV per atom, which is within the error of other approximations made in conventional KS-DFT. This small 40 meV per atom error again confirms that the data points from different bulk structures (Fig. 2) can be interpolated well with smooth curves.

The transferability of our BLPSs can be evaluated by examining the structures not used to fit the BLPSs. For example, the hcp structure is not used to build either the Mg or the Al BLPS. Our BLPSs are able to accurately reproduce the small energy difference between the hcp and fcc structures. Like Zhou *et al.*,[22] we believe that the origin of good transferability exhibited by our BLPSs is because they are constructed from bulk rather than atomic densities. BLPSs are built from bulk environments where the valence electrons are polarized upon bonding to neighboring atoms and experience a change in potential compared to the isolated atom. Our BLPSs explicitly capture changes in potential necessary for good transferability. Overall, our BLPSs for Mg and Al perform better than Madden and coworkers' LPS for Mg[25] and Goodwin *et al.*'s LPS for Al,[19] at least for the properties investigated here. This enhanced performance is not surprising, since Madden and coworkers' LPS makes use of an orbital-free KEDF in its construction, which is a source of error, and Goodwin *et al.*'s LPS is an empirical one fitted only to the experimental lattice parameters of fcc Al and zincblende AlAs.

5.2.2 Surfaces and vacancies. Since our BLPSs are built completely from data from perfect bulk crystals, calculations of the energies of low-index Mg and Al surfaces, as well as vacancy energetics, further challenge the transferability of the

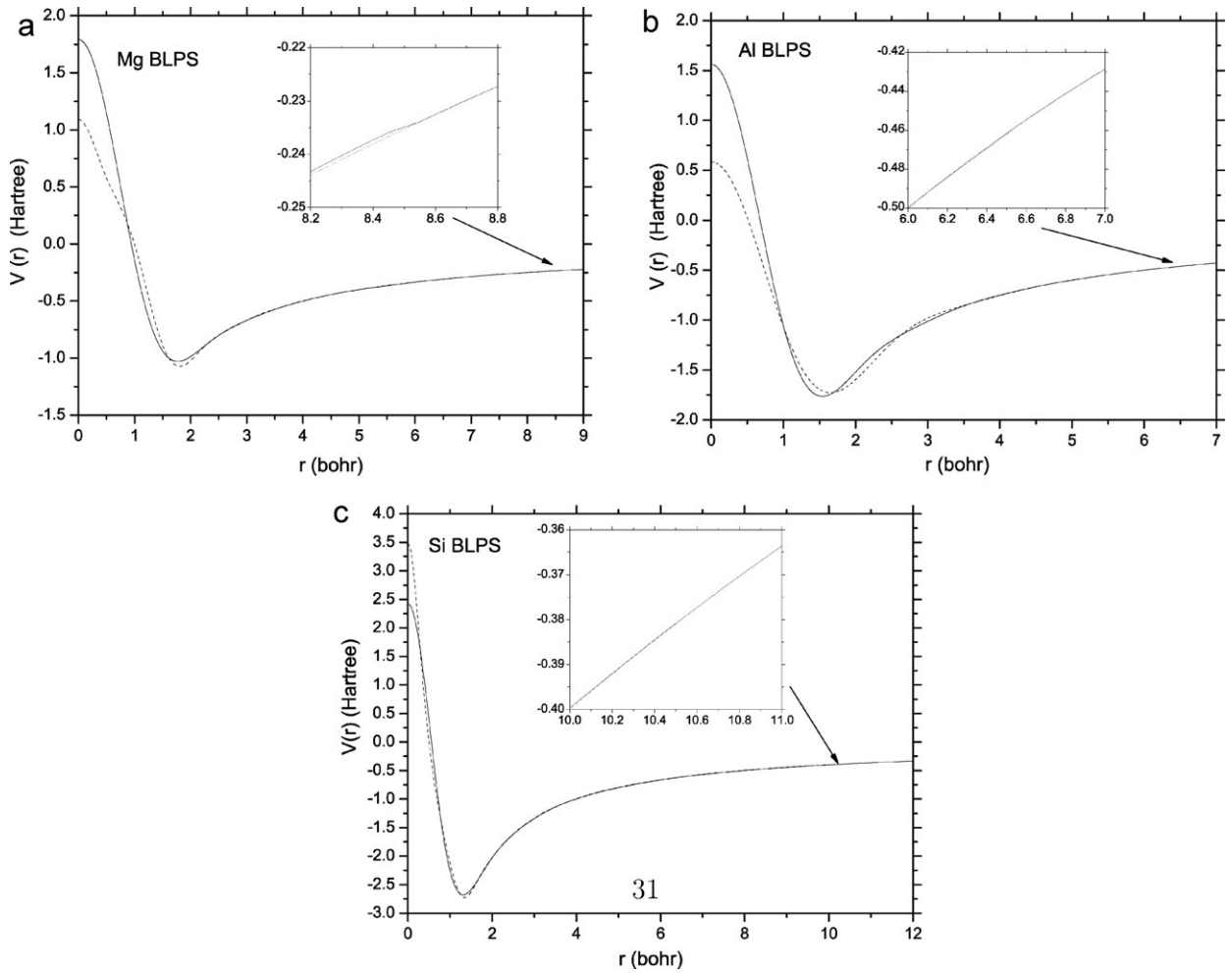

Fig. 3 (a) Mg, (b) Al and (c) Si BLPSs (solid lines) in real space. Madden and coworkers' Mg LPS,[25] Goodwin and coworkers' Al LPS,[19] Zhou and coworkers' Si BLPS (all in dashed lines) are shown together with our Mg, Al, and Si BLPSs, respectively. We see that our new Si BLPS is "softer" than Zhou and coworkers' Si BLPS, whereas our Mg and Al BLPSs are "harder" than those derived empirically (Goodwin and coworkers'[19]) or *via* OF-DFT inversion (Madden and coworkers[25]). The Coulombic tails of the Mg, Al, and Si BLPSs start at 8.5, 6.5, and 10.5 bohr, respectively (see insets).

BLPSs. An atom in a surface layer bonds to the atoms underneath but has no bonds on the vacuum side. So a surface represents a special environment intermediate between the bulk crystal and an isolated atom. The presence of a vacancy represents another case of undercoodination relative to a perfect crystal. As shown in Table 3, the Al BLPS and TM-NLPS predicted surface energies are the same to within $\sim$20 mJ m^{-2}, corresponding to a BLPS error of $\sim$8 meV per atom, well within the expected error of KS-DFT-LDA. This analysis conservatively ascribes all the error to the description of the atoms at the surface, which is a reasonable assumption, given that the bulk crystal is so well described by the Al BLPS. Of course, if we assumed the error was distributed over the non-surface atoms also, the error on a per atom basis would be even smaller. Similarly, the Mg TM-NLPS surface energies for three Mg surfaces are reproduced to within $\sim$10 mJ m^{-2} with our Mg BLPS, corresponding to a $\sim$7 meV per atom error in the BLPS by the same analysis.

We find similarly good agreement between the TM-NLPS and BLPS predictions for Mg and Al vacancy energetics (Table 4). Vacancy formation energies agree to within $\sim$20 meV per vacancy for Mg and $\sim$4 meV per vacancy for Al, while vacancy migration energies differ by no more than $\sim$11 meV per vacancy for Mg and $\sim$26 meV per vacancy for Al. All these deviations between the TM-NLPS and our BLPS are within the expected accuracy of the numerical and physical approximations made in KS-DFT-LDA. By contrast, Madden and coworkers' Mg LPS[25] and Goodwin *et al.*'s Al LPS[19] yield significantly larger discrepancies for the same quantities.

5.2.3 Stacking fault energies in fcc Al. We further test our Al BLPS by calculating various stacking fault energies in fcc Al. As shown in Table 5, our Al BLPS reproduces the TM-NLPS twinning energy very well. Other stacking fault energies predicted by the Al BLPS are all $\sim$50 mJ m^{-2} smaller than those from the TM-NLPS, as seen more clearly in Fig. 4. Assuming the Al BLPS accurately describes the Al atoms away from the stacking fault interface, and ascribing the entire error of $\sim$50 mJ m^{-2} to the less accurate description of the Al atoms at the stacking fault interface, then the Al BLPS error is only

Table 2 KS-DFT-LDA results for bulk moduli (B_0 in GPa), bulk equilibrium volumes (V_0 in Å^3) and equilibrium total energies (E_{min} in eV per atom) calculated using a TM-NLPS, Mg BLPS, and Madden and coworkers' LPS[25] for Mg (upper table). The lower table compares the same quantities using a TM-NLPS, Al BLPS, and Goodwin *et al.*'s LPS[19] for Al. The equilibrium total energies of hcp Mg and fcc Al structures are given, while for all other structures, the energy differences between them and the ground state structures are shown. The TM-NLPS data should be viewed as the benchmark. The new BLPSs perform better overall than previous LPSs

		hcp	fcc	bcc	sc	dia
Mg						
B_0	TM-NLPS	38.6	37.6	37.7	24.6	12.5
	BLPS	38.4	37.5	36.9	29.1	12.7
	Madden LPS	36.2	35.2	34.6	24.2	11.9
V_0	TM-NLPS	42.511	21.429	21.223	25.595	74.373
	BLPS	42.351	21.363	21.393	24.929	71.745
	Madden LPS	44.398	22.432	22.314	26.722	76.081
E_{min}	TM-NLPS	−24.515	0.014	0.030	0.400	0.822
	BLPS	−24.678	0.011	0.033	0.370	0.863
	Madden LPS	−24.400	0.014	0.019	0.351	0.737
		fcc	hcp	bcc	sc	dia
Al						
B_0	TM-NLPS	83.5	80.4	73.8	61.9	41.5
	BLPS	84.0	81.0	76.0	64.3	43.3
	Goodwin LPS	68.2	66.7	62.0	54.9	39.6
V_0	TM-NLPS	15.539	31.319	15.943	19.030	51.943
	BLPS	15.623	31.534	16.063	18.825	51.392
	Goodwin LPS	16.346	33.066	16.779	18.975	49.709
E_{min}	TM-NLPS	−57.207	0.038	0.106	0.400	0.819
	BLPS	−57.955	0.038	0.087	0.362	0.819
	Goodwin LPS	−58.339	0.029	0.071	0.250	0.599

Table 3 KS-DFT-LDA results for the surface energies (in mJ m^{-2}) of Mg hcp(0001), bcc(110), and bcc(001) surfaces (upper table) and fcc Al (110), (100), and (111) surfaces (lower table). The TM-NLPS results should be viewed as the benchmark. Our Mg and Al BLPSs yield significantly more accurate surface energies than Madden and coworkers' LPS for Mg and Goodwin *et al.*'s LPS for Al

Mg	hcp(0001)	bcc(110)	bcc(001)
Mg TM-NLPS	629	680	801
Mg BLPS	631	674	808
Madden LPS	597	601	730
Al	fcc(111)	fcc(100)	fcc(110)
Al TM-NLPS	1013	1122	1207
Al BLPS	1010	1104	1212
Goodwin LPS	803	917	963

10 meV per atom, which is again within the error of other approximations made in KS-DFT-LDA. The lowering of ~50 mJ m^{-2} in stacking fault energies is consistent with the level of error already reported in Table 2, where TM-NLPS energy differences between different Al structures are reproduced by the Al BLPS with an error of ~40 meV per atom. The Al BLPS appears at first glance to yield better results for surface energies, because the surface energies are about 10 times larger than the stacking fault energies. In fact, for both surface and stacking fault energy calculations, the accuracy of our Mg and Al BLPSs is consistently better than 10 meV per atom. By contrast, previous LPSs yield consistently lower and less accurate surface and stacking fault energies.

Table 4 KS-DFT-LDA results for vacancy formation (E_{vf}, in eV) and migration energies (E_{va}, in eV) in hcp Mg (upper table) and fcc Al (lower table) calculated using Mg and Al BLPSs, as well as Madden and coworkers' LPS for Mg and Goodwin *et al.*'s LPS for Al. As benchmarks (labeled as "NLPS" in the table), we use Mg and Al's TM-NLPSs to calculate the E_{vf}, whereas E_{va} is calculated with Mg and Al's ultrasoft NLPSs in CASTEP.[37] Our Mg and Al BLPS results differ less than 30 meV per defect from the benchmarks

Mg	E_{vf}	E_{va}
Experiment	0.81[a] 0.58[b] 0.79[c] 0.90[d]	
NLPS	0.802	0.430
BLPS	0.822	0.419
Madden LPS	0.706	0.390
Al	E_{vf}	E_{va}
Experiment	0.67 ± 0.03[e]	0.61 ± 0.03[e]
NLPS	0.780	0.664
BLPS	0.784	0.638
Goodwin LPS	0.560	0.429

[a] From ref. 49. [b] From ref. 50. [c] From ref. 51. [d] From ref. 52. [e] From ref. 53.

5.2.4 β''-Al_3Mg alloy. Thus far we have tested our Mg and Al BLPSs for cases which contain only Mg or Al atoms. We next test them in an alloy environment: the Al_3Mg alloy in its β'' phase. Our BLPSs do very well for this mixed system (Table 6). The TM-NLPS results for the bulk modulus and equilibrium volume are reproduced accurately by Mg and Al BLPSs, a clear improvement over previous LPSs. Most encouragingly, the small alloy formation energy calculated with our BLPSs differs by only 0.4 meV/(unit cell) from the

Table 5 KS-DFT-LDA results for various stacking fault energies in fcc Al (in mJ m^{-2}) (twinning energy γ_t, unstable stacking fault energy γ_{us}, intrinsic stacking fault energy γ_{isf}, unstable twinning energy γ_{ut}, extrinsic stacking fault energy γ_{esf}) calculated using our Al BLPS. The benchmark values are calculated using the Al TM-NLPS. We see that Goodwin *et al.*'s Al LPS gives much lower stacking fault energies

	γ_t	γ_{us}	γ_{isf}	γ_{ut}	γ_{esf}
Al TM-NLPS	57	188	140	254	149
Al BLPS	40	143	93	188	105
Goodwin LPS	24	95	68	127	79

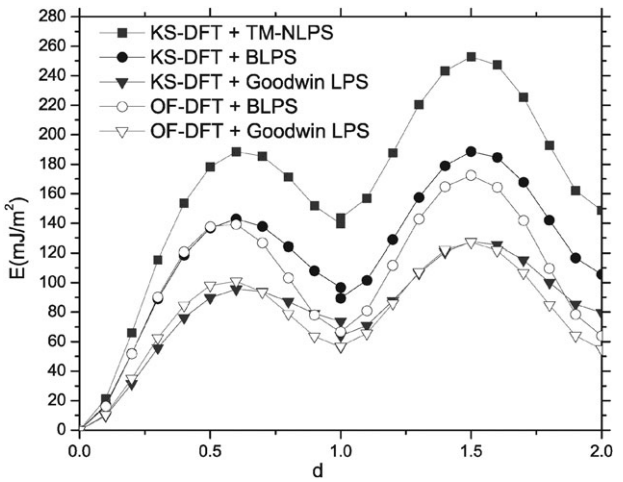

Fig. 4 The stacking fault energy (E, in mJ m^{-2}) as a function of the fractional displacement d. d is the translation (shown in Fig. 1) along the [112] direction with ten $\frac{1}{10}\frac{a}{\sqrt{6}}$ steps (a is the lattice constant of fcc Al at equilibrium). The curves from $d = 0$ to $d = 1$ and from $d = 1$ to $d = 2$ are calculated with the setup (a) and (b) in Fig. 1, respectively. The small discontinuity at $d = 1.0$ is due to the slight difference between setup (a) and (b). Only twin boundaries exist at $d = 0.0$. The unstable stacking fault is formed at $d \approx 0.5$, the intrinsic stacking fault is formed at $d \approx 1.0$, the unstable twinning fault is formed at $d \approx 1.5$, and the extrinsic stacking fault is formed at $d \approx 2.0$.

Table 6 KS-DFT-LDA results for the bulk modulus (B_0 in GPa), equilibrium volume (V_0 in Å^3), and the alloy formation energy (ΔE_f in meV) of the β''-Al_3Mg alloy using Mg and Al TM-NLPSs (as the benchmark), Mg and Al BLPSs, as well as Madden and coworkers' Mg LPS and Goodwin *et al.*'s Al LPS (labeled as "M&G LPSs"). The TM-NLPS results for all properties, including the small alloy formation energy, are accurately reproduced by our BLPSs

	B_0/GPa	V_0/Å^3	ΔE_f/meV per unit cell
Mg&Al TM-NLPSs	70.8	66.440	−8.2
Mg&Al BLPSs	67.5	67.131	−8.6
M&G LPSs	58.0	70.008	−2.7

TM-NLPS prediction. Calculation of the alloy formation energy is the toughest test yet, and we see that the combination of Madden and coworkers' Mg LPS and Goodwin *et al.*'s Al LPS gives a much smaller alloy formation energy.

5.2.5 New Si BLPS. In this work, we make two key improvements on the previous work of Zhou *et al.*:[22] (i) a cutoff function is used to remove the oscillating tail of the BLPS in q-space and (ii) the BLPS's Coulombic tail is systematically determined. The first improvement makes our BLPSs "softer", *i.e.* a smaller kinetic energy cutoff converges the plane wave basis set. The second improvement recovers the intrinsic Coulombic tail of the BLPS, which helps preserve the transferability of the BLPS. With these two refinements, we re-build the Si BLPS with other settings kept the same as in Zhou *et al.*'s work. As shown in Table 7, although Zhou *et al.*'s Si BLPS produces accurate energies and volumes for the common metallic phases (hcp, bcc and fcc), it gives incorrect energy orderings between β-tin and bct5 Si, and between bcc and fcc Si, compared to TM-NLPS predictions. Our new Si BLPS predicts the correct energy ordering for all nine Si structures considered, albeit with some loss of accuracy for the highest energy metallic phases. Our softer Si BLPS produces significantly improved bulk moduli but slightly worse equilibrium volumes for all phases.

We find a mixed outcome for our new Si BLPS compared to Zhou *et al.*'s BLPS when comparing phase transition pressures and defect formation energies to those predicted by the TM-NPLS. Table 8 reveals that our new Si BLPS performs better for the diamond to β-tin phase transition pressure but worse for the diamond to bct5 phase transition pressure, compared to Zhou *et al.*'s Si BLPS. Table 9 shows that our Si BLPS produces smaller defect formation energies than Zhou *et al.*'s Si BLPS, but the difference between self-interstitial and vacancy formation energies is slightly better reproduced by this new Si BLPS.

5.3 OF-DFT tests

Given the status of current KEDFs, OF-DFT is especially suitable for studying main group metals and their alloys, which are nearly-free-electron-like systems. For bulk Al, Mg, and Al_3Mg, it has been shown that the KS-DFT predictions of many key properties can be reproduced very well by OF-DFT when the WGC KEDF is employed.[10,11,40] At present, the accuracy of OF-DFT when applied to these nearly-free-electron-like metals is mainly hindered by the quality of available LPSs.[40,48] We now compare the performance of OF-DFT to KS-DFT using our new Mg and Al BLPSs and the WGC KEDF for all the Mg and Al cases studied above.

5.3.1 Static bulk properties. Various static bulk properties predicted by KS-DFT-BLPS theory are reproduced well by OF-DFT-BLPS theory (Table 10). It is clear that OF-DFT works better for Mg's and Al's fcc and bcc structures than for their diamond and sc structures, since the former are more close-packed, which makes the electron density distributed more evenly, closer to a nearly-free-electron gas. Since the WGC KEDF is based on the latter, it makes sense that the close-packed structures are described more accurately.

5.3.2 Surfaces, vacancies, and stacking faults. OF-DFT with the WGC KEDF does an overall excellent job at describing defects and interfaces in Mg and Al. The errors are all

Table 7 TM-NLPS and our new Si BLPS are used in these KS-DFT-LDA calculations of bulk moduli (B_0 in GPa), equilibrium volumes (V_0 in Å^3), and total energies (E_{min} in eV) for nine phases of Si. The results of Zhou *et al.*'s Si BLPS are quoted from ref. 22. The equilibrium total energy of the Si diamond (dia) structure is given. For other Si structures, the energy differences between them and Si diamond structure are shown. Our new Si BLPS gives a correct energy ordering for all the Si structures, while Zhou *et al.*'s Si BLPS gives incorrect energy orderings between β-tin and bct5, and between bcc and fcc

	dia	hd	cbcc	β-tin	bct5	sc	hcp	bcc	fcc
B_0									
TM-NLPS	96.2	96.2	104.6	117.6	104.1	109.8	91.1	98.0	84.0
BLPS (this work)	98.2	99.3	101.0	121.6	97.4	112.7	95.1	98.0	83.1
Zhou's Si BLPS	95.5	91.5	90.0	106.5	97.5	103.0	83.6	88.6	87.8
V_0									
TM-NLPS	19.476	19.457	17.506	14.694	16.798	15.535	13.687	14.072	13.949
BLPS (this work)	19.777	19.637	17.517	14.663	16.884	15.484	14.157	14.613	14.373
Zhou's Si BLPS	19.432	19.492	17.850	14.880	16.838	15.537	13.858	14.058	14.022
E_{min}									
TM-NLPS	−108.070	0.011	0.122	0.210	0.237	0.278	0.430	0.465	0.482
BLPS (this work)	−109.629	0.014	0.155	0.166	0.210	0.229	0.340	0.351	0.381
Zhou's Si BLPS	−110.234	0.020	0.165	0.275	0.249	0.303	0.447	0.462	0.457

Table 8 Transition pressures (in GPa) calculated with KS-DFT-LDA using the Si TM-NLPS and our new Si BLPS. Results from Zhou *et al.*'s Si BLPS are also listed

	dia → β-tin	dia → bct5
Experiment	12.5[a]	
Si TM-NLPS	7.4	15.6
Si BLPS (this work)	5.4	12.3
Zhou's Si BLPS	10.2	16.6

[a] From ref. 54—experiment estimate.

Table 9 Self-interstitial (E_s) and vacancy (E_v) formation energies in diamond Si, calculated with spin-polarized KS-DFT-LSDA using the default Si ultrasoft NLPS in CASTEP (as the benchmark) and our new Si BLPS. Results from Zhou *et al.*'s Si BLPS[22] are newly calculated in this work. All quantities are in the units of eV/defect

	E_s	E_v	$E_s - E_v$
Others	3.76[a]	3.6[b]	
Si NLPS	3.86	3.67	0.19
Si BLPS (this work)	3.18	3.05	0.13
Zhou's Si BLPS	3.46	3.18	0.28

[a] From ref. 55 spin-restricted KS-LDA, with a larger supercell and a relaxed structure. [b] From ref. 56 and 57—experimental estimate.

<0.1 eV per atom compared to KS-DFT with the same BLPS and often much smaller. For example, OF-DFT predicts the correct energy ordering for different surfaces of both Mg and Al (Table 11). OF-DFT Al surface energies differ by ~240 mJ m^{-2} from the corresponding KS-DFT-BLPS quantities. If we again assume that all the error is due to surface Al atoms, then this 240 mJ m^{-2} deviation indicates an error of ~96 meV per atom. Similarly, OF-DFT reproduces the energy for surface Mg atoms with an error of ~67 meV per atom. As before, these are upper bounds to the per atom error. Secondly, OF-DFT reproduces the KS-DFT-BLPS vacancy formation energies to within ~0.1 eV for Al and ~0.07 eV for Mg (Table 12). Differences between OF-DFT and KS-DFT for vacancy migration energies are <0.03 eV per vacancy for both Mg and Al.

The KS-DFT results (using BLPS) for unstable stacking fault, twinning, and unstable twinning energies are well reproduced by OF-DFT using the WGC KEDF and BLPS (Table 13). On the other hand, the intrinsic (isf) and extrinsic stacking fault (esf) energies from OF-DFT are smaller by 30–40 mJ m^{-2} than predicted by KS-DFT. To understand the origin of the lower isf and esf energies in OF-DFT, note that the formation of either an isf or esf in fcc Al can be thought of as the replacement of one fcc plane by one hcp plane. Table 10 already indicates that the KS-DFT-BLPS energy difference between fcc and hcp Al is about 20 meV per atom higher than from OF-DFT. As discussed above, this 20 meV per atom can lower the isf or esf energies by about 45 mJ m^{-2}. So the smaller isf and esf energies from OF-DFT are largely due to the fact that OF-DFT is still unable to accurately capture the small energy difference between fcc and hcp Al. Consequently, as shown in Fig. 4, the barriers from $d = 1$ to $d = 0$ and from $d = 2$ to $d = 1$ are both 20 meV per atom lower in OF-DFT than those calculated with KS-DFT. This small change of barrier height is on the order of other expected errors in DFT-LDA.

Table 10 Similar to Table 2. OF-DFT-LDA static bulk properties calculated with the WGC KEDF and the BLPS. B_0 is in GPa. V_0 is in Å^3. E_{min} is in eV. KS-DFT-LDA results using the BLPS are repeated from Table 2 for ease of comparison

		hcp	fcc	bcc	sc	dia
Mg						
B_0	OF	36.3	36.2	35.6	27.9	16.0
	KS	38.4	37.5	36.9	29.1	12.7
V_0	OF	43.233	21.465	21.534	25.036	69.579
	KS	42.351	21.363	21.393	24.929	71.745
E_{min}	OF	−24.651	0.006	0.024	0.351	0.860
	KS	−24.678	0.011	0.033	0.370	0.863
		fcc	hcp	bcc	sc	dia
Al						
B_0	OF	80.9	80.0	74.8	62.1	34.4
	KS	84.0	81.0	76.0	64.3	43.3
V_0	OF	15.632	31.529	15.887	19.223	53.247
	KS	15.623	31.534	16.063	18.825	51.392
E_{min}	OF	−57.941	0.018	0.079	0.354	0.827
	KS	−57.955	0.038	0.087	0.362	0.819

Table 11 Similar to Table 3. OF-DFT-LDA surface energies (mJ m^{-2}) calculated with the WGC KEDF. KS-DFT-LDA results from Table 3 are quoted in parentheses for comparison

Mg	hcp(0001)	bcc(110)	bcc(001)
OF (KS)	730 (631)	755 (674)	875 (808)
Al	fcc(111)	fcc(100)	fcc(110)
OF (KS)	1143 (1010)	1343 (1104)	1360 (1212)

Table 12 Similar to Table 4. OF-DFT-LDA vacancy energetics (eV) calculated with the WGC KEDF. The corresponding KS-DFT-LDA results from Table 4 are quoted in parentheses for comparison

Mg	E_{vf}	E_{va}
OF (KS)	0.926 (0.822)	0.396 (0.419)
Al	E_{vf}	E_{va}
OF (KS)	0.854 (0.784)	0.629 (0.638)

Table 13 Similar to Table 5. OF-DFT-LDA stacking fault energies (mJ m^{-2}) for fcc Al, calculated with the WGC KEDF and the BLPS. The corresponding KS-DFT-LDA quantities calculated with the BLPS are shown underneath for comparison

	γ_t	γ_{us}	γ_{isf}	γ_{ut}	γ_{esf}
OF	32	139	67	171	64
KS	40	143	93	188	105

5.3.3 β''-Al$_3$Mg alloy. OF-DFT performs very well for this alloy, as shown in Table 14, independent of which set of LPSs are used. However, our new Mg and Al BLPSs improve the OF-DFT prediction for the alloy formation energy substantially when compared with results obtained using previous LPSs. Moreover, Carling and Carter reported[10] that this small alloy formation energy cannot be correctly reproduced by KEDFs with density-independent response kernels. The WGC KEDF, which is a KEDF with a density-dependent kernel, was the only one to produce this alloy formation energy with the correct sign.[10]

6. Conclusions

In this work, we made two important improvements to Zhou *et al.*'s approach to building BLPSs. We introduced a potential cutoff in Fourier space and systematically determined the cutoff radius beyond which BLPS's Coulombic tail is recovered in real space. Consequently, our new BLPSs are more efficient to use (smaller plane-wave basis expansion required) and more accurate in many instances. We built Mg, Al, and Si BLPSs, and tested their transferability and accuracy by applying them in KS-DFT calculations of static bulk properties of several Mg, Al, and Si bulk structures, defect energetics in hcp Mg, fcc Al, and diamond Si, surface energies for low-index Mg and Al surfaces, and stacking fault energies in fcc Al. Comparison of KS-DFT-BLPS and KS-DFT-NLPS results demonstrated the excellent

Table 14 Bulk modulus B_0, unit cell's equilibrium volume V_0, equilibrium total energy E_0, and alloy formation energy ΔE_f of β''-Al$_3$Mg are calculated using OF-DFT-LDA with the WGC KEDF. The KS-DFT-LDA results are shown in parentheses for comparison. With our BLPSs, the OF-DFT-LDA results for the small alloy formation energy are much improved. "M&G LPSs" refers to the results calculated with Madden and coworkers' and Goodwin *et al.*'s LPSs

OF-DFT	B_0/GPa	V_0/Å^3	E_0/eV per unit cell	ΔE_f/meV per unit cell
Mg&Al BLPSs	66.8	67.144	−198.494	−5.6
	(67.5)	(67.131)	(−198.575)	(−8.6)
M&G LPSs	59.5	69.884	−199.367	−1.7
	(58.0)	(70.008)	(−199.427)	(−2.7)

transferability and accuracy of our BLPSs. In these tests, the error due to the Mg and Al BLPSs is always less than 40 meV per atom, and in most cases is only $\sim$10 meV per atom. These BLPSs are accurate enough in KS-DFT that, in addition to their use in OF-DFT, they could find use in large scale KS-DFT calculations where calculation of NLPS terms can become prohibitively expensive.

We also tested the quality of the WGC KEDF in combination with our new BLPSs by performing OF-DFT calculations for many of the same properties mentioned above. We demonstrated yet again that OF-DFT performs as well as KS-DFT in systems which are close to behaving in a free-electron-like manner.

The method outlined here is ready for use in building BLPSs for other elements for future use in OF-DFT. Moreover, with our improved BLPSs and the WGC KEDF, OF-DFT is now a practical and trustworthy tool for the large-scale simulation of main group metals and their alloys.

Acknowledgements

We are grateful to the National Science Foundation and the Department of Energy for support of this research.

References

1 W. Kohn and L. J. Sham, *Phys. Rev.*, 1965, **140**, A1133.
2 P. Hohenberg and W. Kohn, *Phys. Rev.*, 1964, **136**, B864.
3 S. Goedecker, *Rev. Mod. Phys.*, 1999, **71**, 1085–1123.
4 S. C. Watson and P. A. Madden, *PhysChemComm*, 1998, **1**, 1–11.
5 E. Chacón, J. E. Alvarellos and P. Tarazona, *Phys. Rev. B: Condens. Matter Mater. Phys.*, 1985, **32**, 7868.
6 L.-W. Wang and M. P. Teter, *Phys. Rev. B: Condens. Matter Mater. Phys.*, 1992, **45**, 196.
7 P. García-González, J. E. Alvarellos and E. Chacón, *Phys. Rev. B: Condens. Matter Mater. Phys.*, 1996, **53**, 9509.
8 Y. A. Wang, N. Govind and E. A. Carter, *Phys. Rev. B: Condens. Matter Mater. Phys.*, 1999, **60**, 16350; Y. A. Wang, N. Govind and E. A. Carter, *Phys. Rev. B: Condens. Matter Mater. Phys.*, 2001, **64**, 129901 (erratum).
9 Y. A. Wang and E. A. Carter, in *Theoretical Methods in Condensed Phase Chemistry*, ed. S. D. Schwartz, Progress in Theoretical Chemistry and Physics, Kluwer, Dordrecht, 2000, ch. 5, pp. 117–184.
10 K. M. Carling and E. A. Carter, *Model. Simul. Mater. Sci. Eng.*, 2003, **11**, 339–348.
11 R. L. Hayes, G. Ho, M. Ortiz and E. A. Carter, *Philos. Mag.*, 2006, **86**, 2343–2358.
12 D. R. Hamann, M. Schluter and S. Chiang, *Phys. Rev. Lett.*, 1979, **43**, 1494.
13 D. Vanderbilt, *Phys. Rev. B: Condens. Matter Mater. Phys.*, 1990, **41**, 7892.
14 P. E. Blöchl, *Phys. Rev. B: Condens. Matter Mater. Phys.*, 1994, **50**, 17953.
15 W. C. Topp and J. J. Hopfield, *Phys. Rev. B: Solid State*, 1973, **7**, 1295.
16 J. A. Appelbaum and D. R. Hamann, *Phys. Rev. B: Solid State*, 1973, **8**, 1777.
17 M. Schluter, J. R. Chelikowsky, S. G. Louie and M. L. Cohen, *Phys. Rev. B: Solid State*, 1975, **12**, 4200.
18 T. Starkloff and J. D. Joannopoulos, *Phys. Rev. B: Solid State*, 1977, **16**, 5212.
19 L. Goodwin, R. J. Needs and V. Heine, *J. Phys.: Condens. Matter*, 1990, **2**, 351.
20 F. Nogueira, C. Fiolhais, J. He, J. P. Perdew and A. Rubio, *J. Phys.: Condens. Matter*, 1996, **8**, 287.
21 B. Wang and M. J. Stott, *Phys. Rev. B: Condens. Matter Mater. Phys.*, 2003, **68**, 195102.
22 B. Zhou, Y. A. Wang and E. A. Carter, *Phys. Rev. B: Condens. Matter Mater. Phys.*, 2004, **69**, 125109.
23 B. Zhou and E. A. Carter, *The Journal of Chemical Physics*, 2005, **122**, 184108.
24 J.-D. Chai and J. D. Weeks, *Phys. Rev. B: Condens. Matter Mater. Phys.*, 2007, **75**, 205122.
25 S. Watson, B. J. Jesson, E. A. Carter and P. A. Madden, *Europhys. Lett.*, 1998, **41**, 37.
26 J. A. Anta and P. A. Madden, *J. Phys.: Condens. Matter*, 1999, **99**, 6099.
27 Y. Wang and R. G. Parr, *Phys. Rev. A: At., Mol., Opt. Phys.*, 1993, **47**, R1591.
28 Q. Wu and W. Yang, *J. Chem. Phys.*, 2003, **118**, 2498–2509.
29 X. Gonze, J.-M. Beuken, R. Caracas, F. Detraux, M. Fuchs, G.-M. Rignanese, L. Sindic, M. Verstraete, G. Zerah, F. Jollet, M. Torrent, A. Roy, M. Mikami, P. Ghosez, J.-Y. Raty and D. C. Allan, *Comput. Mater. Sci.*, 2002, **25**, 478–492, http://www.abinit.org.
30 http://www.ece.northwestern.edu/$\sim$rwaltz/CG+.html.
31 G. S. Ho, V. Ligneres and E. A. Carter, *Comput. Phys. Commun.*, 2008, DOI: 10.1016/j.cpc.2008.07.002.
32 D. M. Ceperley and B. J. Alder, *Phys. Rev. Lett.*, 1980, **45**, 566.
33 J. P. Perdew and A. Zunger, *Phys. Rev. B: Condens. Matter Mater. Phys.*, 1981, **23**, 5048.
34 N. Troullier and J. L. Martins, *Phys. Rev. B: Condens. Matter Mater. Phys.*, 1991, **43**, 1993.
35 M. Fuchs and M. Scheffler, *Comput. Phys. Commun.*, 1999, **119**, 67.
36 L. Kleinman and D. M. Bylander, *Phys. Rev. Lett.*, 1982, **48**, 1425–1428.
37 S. J. Clark, M. D. Segall, C. J. Pickard, P. J. Hasnip, M. J. Probert, K. Refson and M. C. Payne, *Zeitschrift fuer Krystallographie*, 2005, **220**(5–6), 567–570.
38 H. J. Monkhorst and J. D. Pack, *Phys. Rev. B: Solid State*, 1976, **13**, 5188.
39 F. D. Murnaghan, *Proc. Natl. Acad. Sci. U. S. A.*, 1944, **30**, 244.
40 G. Ho, M. T. Ong, K. J. Caspersen and E. A. Carter, *Phys. Chem. Chem. Phys.*, 2007, **9**, 1–16.
41 N. Chetty, M. Weinert, T. S. Rahman and J. W. Davenport, *Phys. Rev. B: Condens. Matter Mater. Phys.*, 1995, **52**, 6313.
42 M. J. Gillan, *J. Phys.: Condens. Matter*, 1989, **1**, 689.
43 N. Govind, M. Petersen, G. Fitzgerald, D. King-Smith and J. Andzelm, *Comput. Mater. Sci.*, 2003, **28**, 250.
44 G. Henkelman, G. Johannesson and H. Jónsson, *J. Chem. Phys.*, 2000, **113**, 9901.
45 G. Henkelman, G. Johannesson and H. Jónsson, *Prog. Theor. Chem. Phys.*, 2000, **5**, 269.
46 N. Bernstein and E. B. Tadmor, *Phys. Rev. B: Condens. Matter Mater. Phys.*, 2004, **69**, 094116.
47 *MATLAB, release 14*, The MathWorks, Inc., Natick, MA, 2005. We used the function: pchip.
48 R. L. Hayes, M. Fago, M. Ortiz and E. A. Carter, *Multiscale Model. Simul.*, 2005, **4**, 359.
49 C. Mairy, J. Hillairet and D. Schumacher, *Acta Metall.*, 1967, **15**, 1258.
50 C. Janot, D. Malléjac and B. Georg, *Phys. Rev. B: Solid State*, 1970, **2**, 3088.
51 P. Tzanetakis, J. Hillairet and G. Revel, *Phys. Status Solidi B*, 1976, **75**, 433.
52 A. Vehanen and K. Rytsölä, *Proceedings of the International School of Physics*, North-Holland, Utrecht, 1981.
53 P. Erhart, P. Jung, H. Schult and H. Ullmaier, *Atomic Defects in Metals*, Vol. 25 of Landolt-Börnstein, New Series, Springer-Verlag, Berlin, Heidleberg, 1991.
54 B. A. Weinstein and G. J. Piermarini, *Phys. Rev. B: Solid State*, 1975, **12**, 1172.
55 R. J. Needs, *J. Phys.: Condens. Matter*, 1999, **11**, 437.
56 G. D. Watkins and J. W. Corbett, *Phys. Rev. A*, 1964, **134**, 1359.
57 S. Dannefaer, P. Mascher and D. Kerr, *Phys. Rev. Lett.*, 1986, **56**, 2195.

